Joule

CellPress

Article

Chemically Sustainable Large Stokes Shift Derivatives for High-Performance Large-Area Transparent Luminescent Solar Concentrators

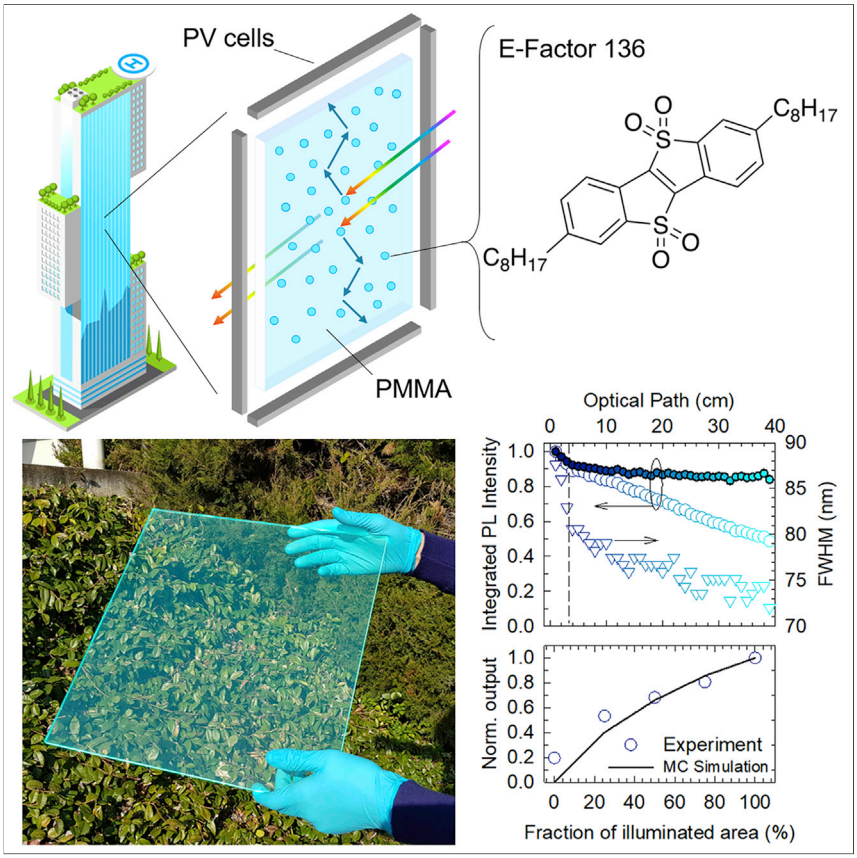

Efficient and aesthetically pleasing solar technologies, such as LSC photovoltaic windows, are becoming essential for the widespread of zero-energy buildings. The more the LSC technology gains appeal, the higher the need becomes for efficient and sustainable materials and production routes. Through a new mechanochemical route, we produce efficient, reabsorption-free LSC emitters with a massively increased sustainability factor. The integration of such derivatives into industrial-grade LSCs leads to an optical efficiency of 3% for large-area devices.

Sara Mattiello, Alessandro Sanzone, Francesco Bruni, ..., Mauro Sassi, Sergio Brovelli, Luca Beverina

sergio.brovelli@unimib.it (S.B.)
luca.beverina@unimib.it (L.B.)

HIGHLIGHTS

A solvent-free mechanochemical route lowers the sustainability factor for LSC emitters

Compatibility with industrial processes leads to optical-grade reabsorption-free LSCs

Large-area transparent LSCs reach an optical efficiency of 3% (54% quantum efficiency)

Mattiello et al., Joule 4, 1988–2003
September 16, 2020
https://doi.org/10.1016/j.joule.2020.08.006

CellPress

Joule

Article

Chemically Sustainable Large Stokes Shift Derivatives for High-Performance Large-Area Transparent Luminescent Solar Concentrators

Sara Mattiello,[1] Alessandro Sanzone,[1] Francesco Bruni,[2] Marina Gandini,[2] Valerio Pinchetti,[1] Angelo Monguzzi,[1] Irene Facchinetti,[1] Riccardo Ruffo,[1] Francesco Meinardi,[1,2] Giuseppe Mattioli,[3] Mauro Sassi,[1] Sergio Brovelli,[1,2,*] and Luca Beverina[1,4,*]

SUMMARY

Luminescent solar concentrators (LSCs) have recently emerged as valuable candidates for the realization of aesthetically pleasing solar windows for near-zero-energy consumption buildings. The growing demand by the building-integrated photovoltaic sector is urging the development of sustainable production methods that minimize the use of polluting organic solvents and hazardous materials, while still enabling industrial-grade LSCs. Here, we introduce a new class of benzothieno-benzothiophene (BTBT) derivatives as highly efficient reabsorption-free emitters for transparent LSCs featuring high stability and a solvent-free chemical access with sustainability factor as low as 21, 10 to 50 times lower than conventional LSC emitters. By embedding our BTBT emitters in optical-grade polymeric waveguides, we produced large-area (40 cm × 40 cm) LSCs with optical power efficiency as high as 3% (corresponding to an optical quantum efficiency of 54%). These results represent an important advancement toward sustainable solar glazing systems for green architecture.

INTRODUCTION

In the last few years, luminescent solar concentrators (LSCs)[1–3] received rapidly growing attention, owing to important breakthroughs in the design of luminescent materials with suppressed reabsorption losses (typically quantified in terms of a wide Stokes shift), which have enabled the fabrication of efficient large-area devices.[4–7] These advancements have paved the way to the realization of new device concepts for architectural integration of solar technologies, such as LSC-based electrodeless photovoltaic windows that are particularly promising for future near-zero-energy buildings, especially in densely populated areas where the implementation of conventional solar modules is hampered by the high "cost of land." An LSC typically consists of a high optical quality plastic or glass waveguide doped or coated by luminescent materials that absorb sunlight and emit at a longer wavelength (Figure 1A). Since the refractive index, n, of the waveguide is higher than that of the air (typically n~1.5), most of the luminescence (up to ~75% of the total) is guided by total internal reflection to the LSC edges, where it is converted into electricity by efficient solar cells installed along the perimeter.[2,8] This all-optical functioning scheme, together with the unique look of LSCs, makes it ideal for building-integrated photovoltaics.[2,9] In particular, specifically designed transparent or neutral-colored LSCs can be hardly distinguished from standard windows, thus ensuring

Context & Scale

The growing demand for building-integrated photovoltaic technologies for near-zero-energy buildings is motivating the scientific community to develop devices that meet the functional, energetic, and aesthetic needs for sustainable architecture. Luminescent solar concentrators (LSCs) are emerging as valuable solutions to realize aesthetically pleasing semitransparent photovoltaic windows capable of converting urban buildings into energy generators. In this work, we report on efficient, transparent LSCs based on a novel class of reabsorption-free derivatives synthesized through a solvent-free route that massively improves the sustainability factor with respect to the state of the art. Optical-grade polymeric LSCs are produced via industrial methods with an optical power efficiency as high as 3% despite their transparency in the visible region. These results represent an important step forward for sustainable solar glazing systems for environmentally friendly architecture.

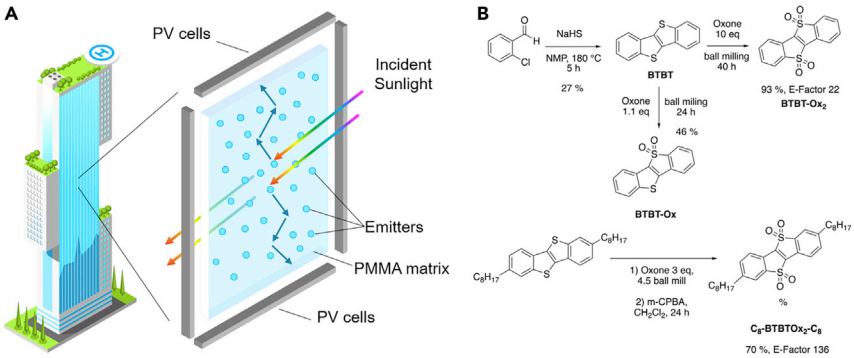

Figure 1. Concept of Highly Sustainable Transparent LSC Window and Reaction Schemes

(A) Schematic depiction of a solar window embedding a transparent luminescent solar concentrator. Solar light penetrates the waveguide and is absorbed by the emitters (blue dots). The photoluminescence (blue arrows) is guided toward the LSC edges, where it is converted into electricity by photovoltaic cells.

(B) Mechanochemical synthesis of **BTBT-Ox**, **BTBT-Ox$_2$**, and **C$_8$-BTBT-Ox$_2$-C$_8$** derivatives.

seamless integration in the building envelope without imposing the aesthetic and fruition constraints of thin-film or laminated photovoltaic (PV) glasses. High-performance LSCs are typically realized using polymethyl methacrylate (PMMA) that features the highest transparency in the visible spectral region among available structural polymers, a particularly stringent requisite for avoiding reabsorption of the propagating luminescence in large-area devices. In terms of the luminescent chromophores, literature reports a wide variety of possible solutions for building-integrated PV (BIPV)-grade LSCs, pertaining to two distinct groups: full-spectrum and transparent. Full-spectrum chromophores are designed to absorb the largest portion of the solar spectrum so as to achieve the highest possible energy output, and typically yield brown- to gray-looking LSCs with sizable absorption (>50% across the UV-vis spectral range).[9–13] These devices are currently mostly based on colloidal semiconductor nanocrystals[5,7,14–17] that enable continuous absorption across the visible and near-infrared solar spectrum and efficient Stokes-shifted luminescence that matches the peak response of silicon solar cells. To date, such an approach has enabled a global record optical power conversion efficiency of 6.8% for large-area (40 cm × 40 cm) LSCs.[7] Schemes based on energy transfer between emitting species have also been proposed.[18–22] Transparent LSCs are not competitive with full-spectrum devices in terms of absolute power conversion efficiency, but they offer the unique benefit of not absorbing visible sunlight, which can become the determining factor for BIPV applications when particularly severe aesthetic or fruition constraints are in place. Transparent LSCs can be realized by employing emitters with selective absorption in the UV, NIR, or both spectral regions. Representative examples[23] are UV-absorbing lanthanide chelates,[24–26] wide-band-gap quantum dots[14,27] and cycloparaphenyles (nCPPs),[28] the latter being the largest Stokes-shift UV-absorbing organic materials so far employed in LSCs. To date, Yang et al. reported the highest internal power conversion efficiency (IPCE = 1.2%) with a transparent, 5 cm × 5 cm, LSC,[29] whereas reabsorption-free LSCs of larger size (20 cm × 25 cm) with optical power conversion efficiency <0.5% was realized with doped perovskite nanocrystals,[27] thus leaving substantial room for further improvements.

The more the LSC technology progresses and gains appeal for the BIPV market, the higher the need becomes for efficient and sustainable materials and production

[1]Dipartimento di Scienza dei Materiali, Università degli Studi Milano Bicocca, via R. Cozzi 55, 20125 Milan, Italy

[2]Glass to Power SpA, via Fortunato Zeni 8, I-38068 Rovereto, Italy

[3]CNR - Istituto di Struttura della Materia, Area della Ricerca di Roma, I-00015 Monterotondo Scalo, Italy

[4]Lead Contact

*Correspondence:
sergio.brovelli@unimib.it (S.B.),
luca.beverina@unimib.it (L.B.)

https://doi.org/10.1016/j.joule.2020.08.006

routes. Along with a high chemical yield, sustainable processes should avoid hazardous chemicals and should feature the lowest possible value of the E-factor, a popular sustainability index consisting of the weight ratio between the total organic waste and the purified product. Concerning the waveguide material, state-of-the-art devices are currently being fabricated via *in-situ* cell casting polymerization of methyl methacrylate monomer, which produces nearly no side products. Nevertheless, more sustainable polymers than PMMA are being actively investigated[30,31] and so is the use of recycled PMMA. On the other hand, very little efforts have been dedicated so far to the development of sustainable emitters for LSCs. Restricting to the class of the organic derivatives, the case of Lumogen R305, the archetypal LSC molecular dye,[32] is particularly instructive. Lumogen R305 is typically prepared in 3 steps starting from perylene-3,4,9,10-tetracarboxylic dianhydride.[33] The overall synthesis yield is ~60%, yet, perylene derivatives are poorly soluble and the second and third synthesis steps require chromatographic purification. Both such features result in the ample use of organic (in this case chlorinated) solvents. Since sustainability aspects have only recently been considered by the scientific literature concerning organic dyes,[34] it is difficult to directly evaluate the E-factor for literature reactions, as the amounts of solvents employed in the purification protocols are generally not reported. For this reason, we prepared a sample of Lumogen R305 following the literature procedure[35] and estimated an E-Factor > 1,000 (see Supplemental Information). Of course, the value corresponding to the industrial synthesis of the dye would be significantly smaller. We decided to carry out the protocol on a lab scale in order to have a fair comparison with the synthesis of **BTBT-Ox$_2$** derivatives performed on the same scale. Scaling up generally improves sustainability by reducing the volumes of the employed solvents. As such, reduction would also apply for **BTBT-Ox$_2$** scaled up syntheses, the advantages of the latter with respect to Lumogen R305 would still be evident. The accepted standard for sustainable processes in the pharmaceutical industry, a sector featuring comparably articulated multistep synthetic processes, is E-factor < 100.[36]

Sustainability can be achieved by improving the synthetic protocols, as testified by the impressive results obtained by applying the concepts of micellar catalysis to the synthesis of organic semiconductors.[34,37,38] A more drastic approach involves the *de novo* design of fluorophores specifically devised to be both efficient and sustainable. Specifically, an ideal candidate should simultaneously possess: (1) accessibility from abundant raw materials through efficient and sustainable synthetic processes; (2) low oxygen sensitivity (i.e., to be electron-poor); (3) thermal- and photo-chemical stability; (3) highly efficient fluorescence; (4) a wide Stokes shift, so as to minimize reabsorption losses; and finally, (5) perfect compatibility with industrially processed polymeric matrices. Efficient fluorophores are typically characterized by an extended conjugation. Among the various available conjugated bridges, polyacenes and their heteroaromatic analogs offer a low energy gap and high stability. [1]benzothieno[3,2-b][1]benzothiophene (BTBT) represents a particularly popular structural motif due to its simple synthetic access (E-factor around 10, see Supplemental Information), availability of efficient routes for late-stage functionalization and high thermal, chemical, and photochemical stability, as endorsed by a dominating position in the literature dedicated to organic thin-film transistors. On the other hand, BTBT is essentially non-fluorescent, electron-rich, and thus, potentially oxygen sensitive and very poorly soluble.

Here, we overcome such limitations by demonstrating a mechanochemical synthesis route for a class of BTBT derivatives simultaneously featuring a very low E-factor, high thermal- and photo-chemical stability, near unity luminescence efficiency,

and minimal reabsorption losses, owing to a large Stokes shift. Crucially, such moieties are also perfectly dispersible into PMMA produced via state-of-the-art industrial routes, which enabled us to fabricate LSCs with an optical power efficiency (OPE) as high as 3.0% (corresponding to an optical quantum efficiency [OQE] of 54%), which is the highest efficiency reported to date for large-area (~ 40 cm × 40 cm) transparent LSC devices.

RESULTS AND DISCUSSION

Design and Mechanochemical Synthesis

The literature on BTBT functionalized derivatives is now vast, including both symmetric and nonsymmetric derivatives, mostly designed in order to tune solubility and/or packing in the solid state.[39] The introduction of reactive side chain moieties that can be further exploited for grafting on a surface or polymerization is also documented.[40,41] Functionalization with either electron-donating or electron-withdrawing groups enabling the tuning of the optoelectronic properties is more seldom reported. Moreover, the literature does not report BTBT derivatives with high luminescence. Aiming at sizably lowering both HOMO and LUMO energies, in order to improve stability toward oxidation and to increase the luminescence efficiency by reducing the tendency to π-stack, we took inspiration from a strategy proposed for oligothiophene molecular semiconductors: the oxidation of the sulfur atoms to sulfone. A series of now classical papers from Barbarella et al. demonstrated that the oxidation of one or more of the sulfur atoms of oligothiophene derivatives is a resourceful strategy to turn a native *p*-type semiconductor into an *n*-type one.[42,43] Moreover, the oxidation results in a remarkable increase in the luminescence efficiency, both in solution and in the solid state.[42] Recent computational results suggested a similar behavior also for BTBT derivatives.[44] The common method to perform such oxidation requires the use of m-chloroperbenzoic acid (m-CPBA) as the oxidizer in a chlorinated solvent solution. In the case of BTBT, the reaction is moderately efficient, leading to the formation of the target **BTBT-Ox$_2$** compound in 72 h at room temperature, in a yield of 54%. Unfortunately, due to the very low solubility of BTBT in organic solvents, the reaction requires unusually large amounts of toxic chlorinated solvents. Conversely, purification is straightforward as a single crystallization from dimethyl sulfoxide affords analytical samples. The E-factor for this transformation alone is 211 (see Supplemental Information for details), a rather large value for such a simple derivative (Figure 1B). The solvent is by far the heaviest item in the organic waste list for this reaction. The only other **BTBT-Ox$_2$** synthesis described in the literature involves a potentially hazardous exothermic *in-situ* generation of a warm peracetic acid/diacetyl peroxide and is therefore not advantageous.[45] We thus performed a solvent-less oxidation using Oxone® (potassium peroxymonosulfate) as the oxidizer under mechanochemical conditions in a ball miller. Mechanochemical reactions are gaining increasing interest as intrinsically sustainable and industrially scalable procedures[46] Remarkably, the reaction became more efficient, and in contrast to what we observed for the m-CPBA-mediated oxidation, it could be selectively oriented toward the formation of the S,S-dioxide (**BTBT-Ox**) versus the target S,S,S′,S′-tetraoxide (**BTBT-Ox$_2$**) simply by changing the amount of Oxone® employed (Figure 1C). The isolation of the product simply requires suspension in water of the crude milling residue until the complete dissolution of all salts. The derivative **BTBT-Ox** requires further crystallization from toluene, while the analytically pure **BTBT-Ox$_2$** is recovered simply by filtration and vacuum drying. The reaction produces no organic waste, yet, in this case, the excess of Oxone® has to be taken into account in the estimate of the still remarkably small E-factor of 21. **BTBT-Ox$_2$** solubility in organic solvents is very poor; as such, we also prepared

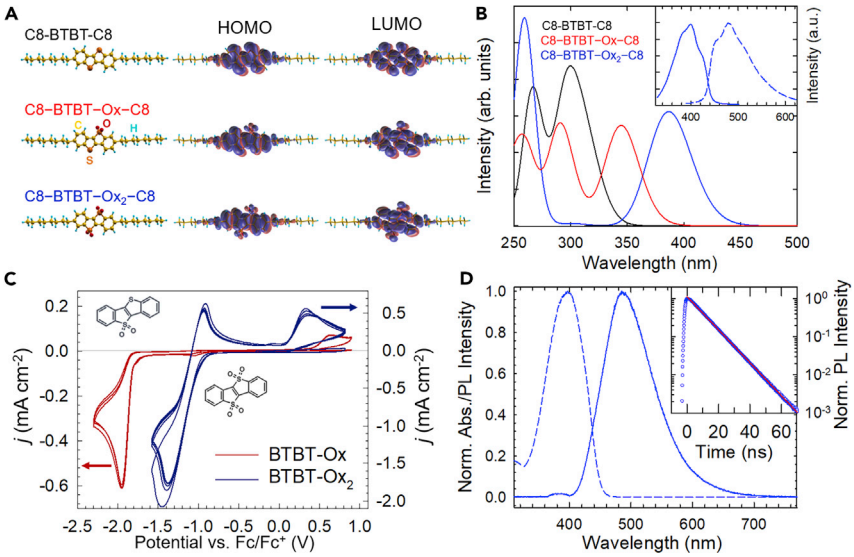

Figure 2. Theoretical Modeling and Electro-Optical Characterization

(A and B) (A) Optimized geometries and frontier orbitals of **C8-BTBT-C8** and of its **C8-BTBT-Ox-C8** and **C8-BTBT-Ox$_2$-C8** derivatives, (B) respective TDDFT (B3LYP) absorption spectra. The inset contains the vibrational structure of the lowest-energy singlet absorption (full curve) and fluorescence (dashed curve) transitions of **C8-BTBT-Ox$_2$-C8**, calculated by using the IMDHO method as detailed in the experimental part.

(C) Cyclovoltammograms of **BTBT-Ox** (red curve) and **BTBT-Ox$_2$** (blue curve). The solutions are 5 × 10^{-3} M in 0.1 M $(Bu_4N)ClO_4/CH_2Cl_2$, the working electrode selected is gassy carbon pin and the scanning speed is 50 mVs^{-1}.

(D) Optical absorption (dashed line) and photoluminescence (solid line) of a 0.9 × 10^{-6} M solution of **C$_8$-BTBT-Ox$_2$-C$_8$** in CH_2Cl_2. **Inset**: photoluminescence kinetics the same solution upon excitation with a 405 nm pulsed laser at room temperature.

the solubilized analogous **C$_8$-BTBT-Ox$_2$-C$_8$**. In this case, we used a mixed mechano-chemical/m-CPBA procedure as the **C$_8$-BTBT-C$_8$** precursor is not fully stable to very large Oxone excesses. The overall yield and E-factor are 70% and 138, to be compared with the 50% yield and E-factor of 1,650, obtained with a purely organic solvent-based method, respectively (see Figures S1–S10).

Modeling of the Electronic Properties

The structural, electronic, and optical properties of **BTBT**, **BTBT-Ox**, and **BTBT-Ox$_2$** derivatives and the alkylated counterparts were first investigated by using *ab-initio* simulations based on the density functional theory (DFT). All systems feature a rigid and planar structure with high delocalization of the molecular orbitals (Figure 2A). The introduction of two versus four oxygens on the sulfur atoms relates to a major redistribution of the electron density from the conjugated backbone to the sulfur atoms. The UV-vis absorption spectra for the three derivatives calculated by applying a 3,000 cm^{-1} Gaussian broadening to the calculated transition frequencies and oscillator strengths are shown in Figure 2B. The progressive oxidation of sulfur atoms lowers the energy gap, as testified by the calculated energies of the HOMO and LUMO levels for all derivatives reported in Table 1. Notably, the oxidation downshifts both frontier levels to the point that, for **C8-BTBT-Ox$_2$-C8**, the LUMO level is essentially aligned to that of $PC_{61}BM$, the prototypical *n*-type semiconductor employed in solution-processed solar cells. For the derivative **C8-BTBT-Ox$_2$-C8** that features the smallest energy gap in the series, while remaining essentially UV absorbing, DFT calculations also predict a particularly large Stokes shift between

Table 1. The Structural, Electronic, and Optical Properties of BTBT Derivatives

	C8-BTBT-C8	C8-BTBT-Ox-C8	C8-BTBT-Ox_2-C8	$PC_{61}BM$
HOMO				
TPSSh	−5.36	−5.79	−6.16	−5.71
B3LYP	−5.50	−6.02	−6.49	−5.89
CAM-B3LYP	−6.86	−7.43	−7.94	−6.98
LUMO				
TPSSh	−1.66	−2.46	−3.28	−3.60
B3LYP	−1.29	−2.07	−2.89	−3.36
CAM-B3LYP	−0.21	−0.98	−1.80	−2.61
HOMO-LUMO gap				
TPSSh	3.70	3.33	2.88	2.11
B3LYP	4.21	3.95	3.60	2.53
CAM-B3LYP	6.65	6.45	6.14	4.37
S0→S1 (nm)	315	345	387	N/A
Stokes Shift (cm^{-1})	N/A	N/A	4,182	N/A
	BTBT	BTBT-Ox	BTBT-Ox_2	
M/M+ (CH_2Cl_2, V)	−5.54	−5.99	−6.36	N/A
M/M- (CH_2Cl_2, V)	−1.99	−2.82	−3.85	N/A

Values are given in eV, unless otherwise stated. The electronic properties of $PC_{61}BM$ have been also added to the table for comparison.

the absorption and the photoluminescence (PL) spectra, as shown in the inset of Figure 2B.

Electrochemical Characterization

We carried out the electrochemical characterization of both **BTBT-Ox** and **BTBT-Ox_2** to confirm their electron-deficient character, as assessed by the computational investigation. In Figure 2C, the cyclovoltammogram of **BTBT-Ox** is reported, showing a non-reversible reduction peak at −1.95 V (versus Fc/Fc^+). Conversely, the fully oxidized **BTBT-Ox_2** shows a quasi-reversible reduction peak at less negative potentials (−1.38 V) attributed to an *n*-type process, along with two oxidation peaks at −0.9 and 0.32 V. From the onset of the reduction peak, an absolute electrochemical LUMO potential of −3.9 V was determined. This result is in excellent agreement with the DFT calculations predicting oxidation and reduction potentials of −6.36 and −3.85 V, respectively, thus confirming the efficacy of such an oxidation strategy. The cyclovoltammogram of the alkylated derivatives is shown in Figure S11.

Optical Properties

Having assessed the *n*-type nature of **BTBT-Ox_2** derivatives, we turned to photophysical studies. This study was carried out on the solubilized **C_8-BTBT-Ox_2-C_8** derivative for consistency with all the LSCs data. The presence of the two alkyl chains exerts only a marginal effect on the optical and electrochemical properties of the molecules, as we have fully verified by performing a complete computational and electrochemical study on the alkylated derivatives (included in the Supplemental Information section). **C_8-BTBT-Ox_2-C_8** is soluble enough in MMA to enable the preparation of PMMA slabs by the cell casting method. The derivative features a strong luminescence, a distinctive characteristic generally not observed in other BTBT derivatives, including the parent compound. Figure 2D shows the absorption and PL

spectra of the CH_2Cl_2-solution of the compound. The first absorption band peaks at 400 nm and is separated from the PL band by an 85 nm Stokes shift, in agreement with the DFT calculations. The fluorescence quantum yield (QY) is remarkably high, Φ_{PL}>95%. The PL kinetics of **C_8-BTBT-Ox_2-C_8** is perfectly single exponential with lifetime τ = 10 ns at room temperature (Figure 2D, inset). Such performance places **C_8-BTBT-Ox_2-C_8** among the most efficient organic emitters operating within the same optical window. It should be noted that, despite the rigidity of the molecular structure, the typical vibronic replicas are not distinguishable because of the spectral broadening typical of donor-acceptor molecules.

Highly Efficient Transparent LSCs

In order to experimentally validate the potential of our sustainable BTBT derivatives for LSCs, we employed the cell casting method[25,47,48] to fabricate industrial-grade large-area (40 cm × 40 cm) devices based on **C_8-BTBT-Ox_2-C_8** doped into PMMA. Figure 3A shows two photographs of the prototype semitransparent LSC highlighting the transparency in the visible spectral region and showing sizable PL emitted from the device edges already under ambient illumination. A relatively low emission is observed from the top and bottom surfaces, indicating that optical losses by light scattering are minimal, consistent with the high solubility of the compound into PMMA. The transmitted light presents a color-rendering index CRI = 94.4, correlated color temperature CCT = 5,777.2 K, and Commission Internationale de l'Eclairage (CIE) color coordinates of x = 0.326 and y = 0.357. To quantitatively assess the absence of scattering losses, we performed PL measurements in an integrating sphere on the same nanocomposite, with either clear or blocked edges so as to discriminate between the light emitted from the LSC faces and the guided PL emitted from the slab edges. The PL data reported in Figure 3B show that the emission intensity of the LSC with blocked edges corresponds to 29% of the total emission intensity measured for the bare LSC. This indicates that the luminescence guided to the device edges is 71% of the total light generated inside the waveguide, which within the experimental error, matches well the maximum theoretical value of light-trapping efficiency defined by Snell's law, η_{tr} = 0.741 (considering the refractive index of the PMMA matrix, n = 1.49).[2] These results further indicate that optical losses due to reabsorption are very limited, as isotropic reemission events typically lower η_{tr} by randomizing the propagation path of the guided PL.

A further relevant aspect of LSC waveguides produced by the cell-casting polymerization using radical initiators is the preservation of the native optical properties of the chromophore. The absorption and emission profiles of the slab are shown in Figure 3C in direct comparison with a CH_2Cl_2 solution, highlighting the perfect preservation of the spectral properties and of the large Stokes shift. The respective PL decay traces are reported in Figure 3D, showing perfect single-exponential kinetics also upon incorporation into PMMA. The emission lifetime undergoes a minor acceleration in the slab (from 10 to 9 ns) in perfect agreement with the expected acceleration of the radiative decay rate in PMMA with respect to dichloromethane due to the slightly higher refractive index (1.49 versus 1.42). This confirms that the chemical integrity of **C_8-BTBT-Ox_2-C_8** is unaffected by the radical polymerization, as confirmed by quantitative measurements on the PMMA composite in an integrating sphere, yielding Φ_{PL}>95%.

In order to assess the stability of **C_8-BTBT-Ox_2-C_8** embedded into the PMMA matrix in light of potential application in building-integrated photovoltaic devices, such as PV windows, we monitored the PL intensity of our LSC over time as a function of temperature from 30°C to 80°C, which is the typical temperature range experienced by

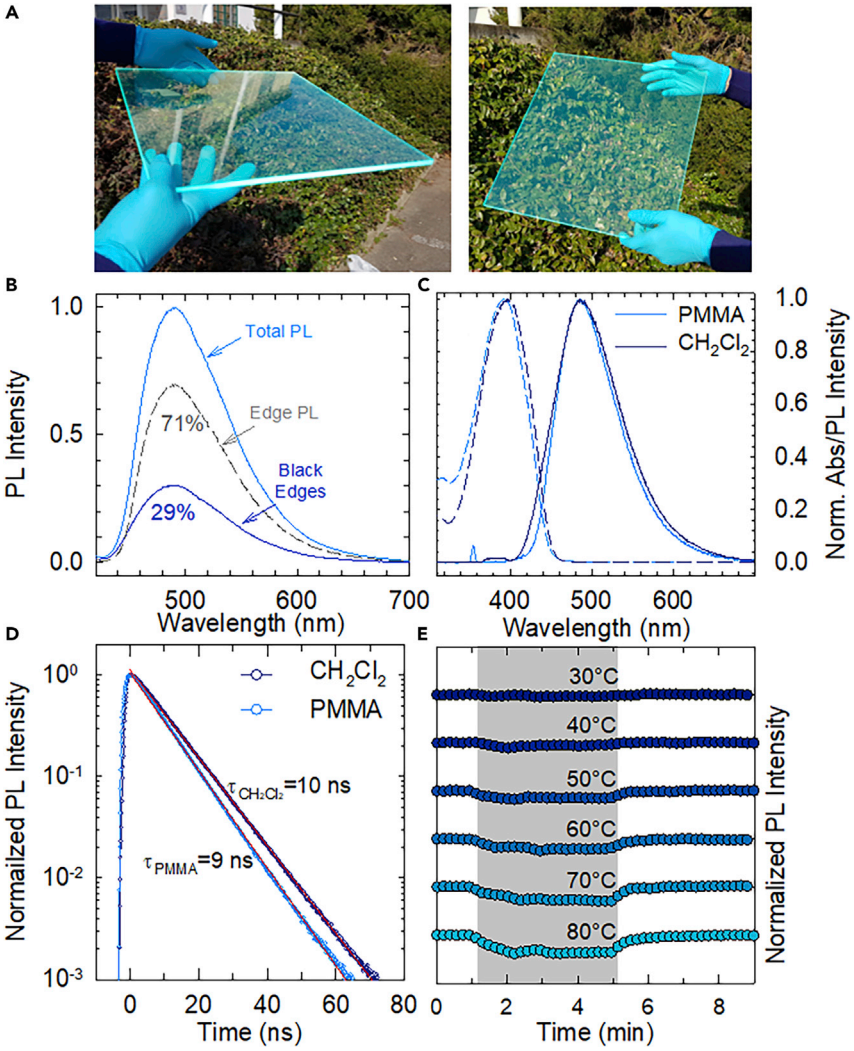

Figure 3. BTBT-PMMA Optical Waveguides

(A) Photographs of a PMMA-based LSC (dimensions of 40 cm × 40 cm × 0.7 cm) under ambient illumination.

(B) PL spectra of a portion of the same LSC as in (A) (dimensions of 3.5 cm × 3.5 cm × 0.7 cm) with the edges clear (light blue line) and blocked by black paint (dark blue line). The gray curve is the difference between the light and dark blue spectra and represents the PL emitted from the device edges.

(C and D) (C) Optical absorption and PL spectra and (D) PL decay curves collected at 500 nm of the LSC compared with the spectra of C_8-BTBT-Ox_2-C_8 in CH_2Cl_2 solution. The red lines are the fits to a single-exponential function.

(E) Normalized PL intensity over time, measured during heating ramps from room temperature (first minute) to the indicated temperature (30°C–80°C, highlighted by the gray shading) and back (last 4 min). The data for the various ramps have been stacked for clarity.

insulated glass units in operative conditions. The data for different ramps is reported in Figure 3E, all starting and finishing at room temperature. Upon raising the temperature, a systematically larger reversible drop of the PL intensity is observed, as expected from increased nonradiative thermal quenching on the Φ_{PL} of C_8-BTBT-Ox_2-C_8. Most importantly, for any temperature tested, the initial PL intensity is perfectly restored after the heating stage, indicating no permanent damage either to the emitter or to the PMMA matrix. We further evaluated the optical stability of

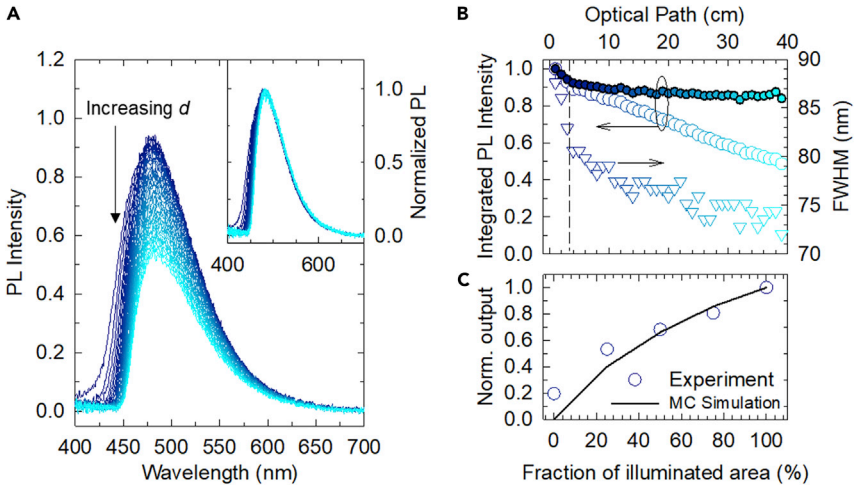

Figure 4. Highly Efficient Transparent LSCs

(A) PL spectra as a function of the distance, d, between the excitation spot and the device edge for a **C_8-BTBT-Ox_2-C_8** containing PMMA LSC. The normalized spectra are shown in the inset to highlight the minimal losses to reabsorption, free from geometrical effects.

(B) The full width at half-maximum (FWHM) and integrated PL intensity versus *d* (empty and full circles for raw and normalized PL spectra, respectively).

(C) Relative optical output power measured from one LSC edge as a function of the illuminated device area. The trend obtained through Monte Carlo simulation of an ideal LSC with no scattering/reabsorption losses and embedding emitters with the same PL quantum efficiency as **C_8-BTBT-Ox_2-C_8** (Φ_{PL} = 95%) is reported as a black curve.

C_8-BTBT-Ox_2-C_8, both in CH_2Cl_2 solution and embedded in the LSC under continuous illumination for 4 h at 400 nm, with fluence equivalent of one sun illumination. The results are displayed in Figure S12 and show that the molecule in solution is very stable and suffers no measurable degradation for the whole duration of the measurement. In turn, the luminescence efficiency of the LSC decreases by ~15%, which is ascribed to the fact that the LSC waveguide was fabricated without stabilizing additives that are commonly used to suppress unreacted radical initiator molecules in the PMMA composite that can be photoactivated by the UV illumination, thus causing photobleaching of embedded chromophores.

One key aspect of our BTBT derivatives is that they combine a sustainable chemical access to stability, high PL efficiency, and a large Stokes shift that suppresses optical losses by reabsorption. To experimentally evaluate the reabsorption losses in our LSC, we collected the PL spectrum at an increasing distance, *d*, between the excitation spot and the slab edge, from where the PL is collected. The PL spectra are reported in Figure 4A. As expected, given the almost complete absence of overlap between the **C_8-BTBT-Ox_2-C_8** absorption and PL spectra, the PL spectra at an increasing *d* are very similar, with the spectrum for d = 40 cm showing only the expected intensity drop based on geometrical effects. The minor role of reabsorption is confirmed by the evolution of the normalized PL spectra reported in the inset of Figure 4A, showing a very small decrease only of the high-energy portion of the spectrum. Such a minimal effect of reabsorption is further quantified by the small variation of the spectral linewidth reported in Figure 4B, together with the integrated emission intensity extracted from the spectra in Figure 4A, showing that reabsorption affects the propagating PL only for the first 3 cm (as highlighted by the vertical dashed line), whereas for longer optical distances the luminescence propagates freely. This is particularly impressive compared with the characteristic

response of high-quality LSCs containing Lumogen Red, whose larger spectral overlap between the absorption and emission profiles leads to optical losses for significantly longer optical distances.[49] As a result of the successful suppression of PL reabsorption by C_8-BTBT-Ox_2-C_8, together with the high optical quality of the waveguides resulting in nearly negligible scattering losses and the high PL efficiency of the emitter, our LSC shows remarkably high performance despite its high transparency in the visible spectra range.

To quantify the efficiency parameters of our LSC, namely, the optical efficiency (OE, evaluated as the number of edge-emitted photons divided by the number of solar photons impinging on the device surface), the OPE (defined as the ratio between the optical power emitted by the LSC and the incident solar power) and the OQE (defined as the ratio between the number of photons emitted from the waveguide edges and the number of absorbed solar photons), we index matched the perimeter edges (A_{edge} =160 cm × 0.7 cm = 112 cm^2) of the LSC shown in Figure 3A to calibrated c-Si solar cells (V_{OC} = 0.7 V, FF = 0.6). We exposed the LSC to outdoors illumination perpendicular to its top surface (A_{LSC} = 40 cm × 40 cm = 1,600 cm^2) and used a calibrated photodiode to instantaneously monitor the solar irradiance impinging onto the LSC top surface. No reflector or back diffuser was placed at the bottom of the waveguide. Based on these measurements, we obtained an OPE = 3.0 ± 0.2%, OE = 2.68%, and a high OQE = 54.3%. Compared with recently reported record LSCs (OPE = 6.8%) of similar large size based on colloidal quantum dots absorbing across the whole visible spectrum,[7] the obtained performance is particularly remarkable, given the higher transparency of the current LSC in the visible spectral region (~10% of the solar power between 380 and 830 nm). The corresponding electrical power conversion efficiency is ~0.7%, which is not far from the highest efficiency for transparent LSCs reported to date (IPCE = 1.2 %) that was obtained for much smaller devices (5 cm × 5 cm) coupled to GaAs PV cells with V_{OC} = 0.99 V and FF = 0.8. To provide an approximate, yet instructive, estimate of the impact that our transparent LSCs could have on the sustainability of real buildings, we calculated that by implementing them in the windows of the One World Trade Centre in New York City (vertical glass surface = 92,903 m^2), one would generate ~0.55 GWh/year, which would be sufficient to power over 180 four-people apartments. It is further important to consider that our transparent LSCs operate with luminescence wavelength in the visible spectral region, which opens the possibility of employing emerging PV technologies, such as perovskite solar cells with V_{OC}~1.5 V spectrally tuned to match the guided luminescence.[50] This combination could substantially boost the single-module efficiency of transparent LSCs to over 3%, increasing the yearly energy production to over 1.65 GWh/year (covering the need of over 500 apartments). Furthermore, also in line with the state-of-the-art LSCs, the effective suppression of reabsorption and scattering losses results in the nearly ideal behavior of the LSC. This is highlighted in Figure 4C, where we show the light output emitted from one of the device edges (40 cm × 0.7 cm) measured using the same setup adopted for the OE measurements (with only one slab edge coupled to the photodiodes and no back reflector) but progressively exposing increasingly larger portions of the LSC area to sunlight. The same figure also shows the trend calculated using Monte Carlo ray-tracing simulation for an ideal LSC free from scattering and reabsorption losses of identical dimensions embedded with emitters of the same quantum efficiency as C_8-BTBT-Ox_2-C_8 (Φ_{PL} = 90%), in which the power output is determined solely by the numeric aperture of the illuminated device area. The experimental and theoretical data are in very good agreement with each other, indicating that our LSC is very close to an ideal device. We notice that the light output due to the first section of the device area (corresponding to one-

quarter of the total surface) is larger than the theoretical prediction, consistent with the small drop of the PL intensity and spectral linewidth (~8%) due to small residual reabsorption shown in Figure 4A.

In summary, we have demonstrated a mechanochemical route to produce a class of BTBT derivatives simultaneously exhibiting high chemical and optical stability, near unity luminescence QY, and a large Stokes shift ensuring reabsorption-free waveguiding in large-area transparent LSCs. Crucially, the synthesis of our derivatives features a remarkably low E-factor averaging between 20 and 200 depending on the substitution pattern, which is unprecedented for any LSC emitters known to date. We finally fabricated state-of-the-art, large-area (40 cm × 40 cm) LSCs using industrial-grade cell-casting methods for high optical quality PMMA waveguides with OPE as high as 3% (corresponding to an OQE of 54%). These results represent an important advancement toward sustainable solar glazing systems for green architecture.

EXPERIMENTAL PROCEDURES

Resource Availability

Lead Contact

Further information and requests for resources and materials should be directed to and will be fulfilled by the Lead Contact, Luca Beverina (luca.beverina@unimib.it)

Materials Availability

All chemicals, unless otherwise specified, were purchased from commercial resources and used as received.

Data and Code Availability

This study did not generate any unique datasets or code.

Materials

All chemicals were purchased from TCI-Europe and used without purification. Milling was performed using a SPEX 8000M Mixer/Mill with a 2.5 × 2.7 in (6.35 cm × 6.83 cm) zirconia vial set (SPEX 8005) using four 0.5 in (12.7 mm) zirconia grinding balls. NMR spectra were recorded on a Bruker Avance wide bore instrument working at 500 MHz for 1H.

Synthesis of S,S-Dioxide Derivatives

[1]Benzothieno[3,2-b]Benzothiophene S,S-Dioxide (BTBT-Ox)

BTBT (4.026 g, 16.75 mmol) and Oxone® (11.35 g, 18.44 mmol) were placed into the milling vial (ZrO_2, V = 45 ml) equipped with four ZrO_2 spheres (d = 15 mm). The jar was sealed with a PTFE gasket and a ZrO_2 lid. After 24 h of milling, the jar was opened, the balls were removed, and water (40 mL) was added. The suspended yellow solid was filtered and dried at 60 °C under reduced pressure. Crystallization from toluene gave the product as a faint yellow powder. (2.080 g, 46%) ^{1}H NMR (500 MHz, $CDCl_3$) δ 8.06 (d, J = 8.45 Hz, 1H), 7.89 (d, J = 8.45Hz, 1H), 7.79 (d, J = 6.65Hz, 1H), 7.61 (dd, J = 8.00,7.5 Hz, 1H), 7.56–7.51 (m, 3H), 7.47 (dd, J = 7.25,7.55 Hz, 1H); ^{13}C NMR (125.70 MHz, $CDCl_3$) δ 144.5, 143.7, 143.4, 134.6, 134.5, 131.2, 131.2, 129.3, 127.7, 127.4, 124.7, 123.3, 123.1, 122.9. Anal calcd for: $C_{14}H_8O_2S_2$: C, 61.74; H, 2.96. Found: C, 61.71; H, 2.99.

[1]Benzothieno[3,2-b]Benzothiophene S,S,S′,S′-Tetraoxide (BTBT-Ox_2)

Method (1). BTBT (1.000 g, 4.161 mmol) and oxone (25.46 g, 41.36 mmol) were placed in a ZrO_2 milling jar (V = 45 mL) equipped with four ZrO_2 spheres (d = 15 mm). The jar was sealed with a PTFE gasket and a ZrO_2 lid and mounted on a

planetary ball mill. After 40 h of milling, the jar was opened, the balls were removed, and water (40 mL) was added. The mixture was filtered, washed with hot water, and dried at 60°C under reduced pressure to afford the pure product (1.180 g, 93%) as a bright yellow powder. ^{1}H NMR (500 MHz, DMSO−d_6, T = 343K) δ 7.93–7.84 (m, 6H), 8.22 (d, J = 6.76Hz, 2H); ^{13}C NMR (125.70 MHz, DMSO−d_6 T = 343 K) δ 141.9, 141.0, 136.8, 134.5, 125.3, 125.2, 123.0. Anal calcd for: $C_{14}H_8O_4S_2$: C, 55.25; H, 2.65. Found: C, 55.18; H, 2.61. E-Factor: 21.

Method (2). BTBT (0.241 g, 0.100 mmol) was dissolved in 20 ml of CH_2Cl_2 and then m-chloroperbenzoic acid (m-CPBA, 77%, 2.260 g, 10.08 mmol) was slowly added. The solution was stirred for 12 h at room temperature. A yellow solid precipitated, which was collected by filtration, washed directly on the filter with a saturated solution of $NaHCO_3$ (50 ml) and water (25 ml), and finally dried in an oven overnight (0.200 g, 66%). E-factor 211.

2,7-Dioctyl-[1]Benzothieno[3,2-b]Benzothiophene S,S,S′,S′- Tetraoxide (C_8-BTBT-Ox_2-C_8)

Method (1). BTBT (0.401 g, 0.863 mmol) and Oxone (1.599 g, 2.598 mmol) were placed in a ZrO_2 milling jar (V = 45 mL) equipped with four ZrO_2 spheres (d = 15 mm). The jar was sealed with a PTFE gasket and a ZrO_2 lid and mounted on a planetary ball mill. After 4.5 h of milling, the jar was opened, the balls were removed, and 10% aqueous $NaHSO_3$ (40 mL) was added. The mixture was filtered and the solid (427 mg) dried at 60 °C under reduced pressure. 212 mg of the crude mixture was submitted to purification by column chromatography (SiO_2, eluent DCM/heptane 1:1 to DCM) to afford an analytical sample of 2,7-dioctyl-[1]benzothieno[3,2-b]benzothiophene S,S-dioxide. ^{1}H NMR (400 MHz, $CDCl_3$) δ 7.92 (dd, 1 H, J = 8.3, 0.6 Hz), 7.66 (m, 1H), 7.59 (m, 1H), 7.37 (m, 2H), 7.34 (dd, 1H, J = 8.30, 1.5 Hz), 4.67–4.76 (m, 4H), 1.66 (m, 4H), 1.27–1.32 (m, 20H), 0.86–0.90 (m, 6H)); ^{13}C NMR (100 MHz, $CDCl_3$) δ 146.1, 143.0, 142.8, 142.6, 141.8, 133.4, 133.1, 128.3, 127.8, 126.1, 122.9, 121.83, 121.79, 121.76, 36.1, 35.9, 31.84, 31.82, 31.5, 31.0, 29.4, 29.3, 29.21, 29.17, 22.6, 14.1. The remaining 215 mg of the crude reaction mixture was dissolved in 10 mL of DCM, and m-chloroperbenzoic acid (m-CPBA, 748 mg, 3.34 mmol) was added stepwise at room temperature. The solution was stirred for 24 h. The white precipitate was removed by filtration and the organic solution was subsequently washed with a 10% aqueous $NaHSO_3$. The solvent was evaporated at reduced pressure and the crude was purified by crystallization (solvent: ethanol) to afford the product as a bright yellow powder (160 mg, 70% overall for the two steps) ^{1}H NMR (500 MHz, $CDCl_3$) δ 7.63 (s, 2H), 7.59 (d, J = 7.9 Hz, 2H), 7.48 (d, J = 7.9 Hz, 2H), 2.74 (t, J = 7.8 Hz, 4H), 2.79–2.67 (m, 4H), 1.70–1.61 (m, 4H), 1.20–1.40 (m, 20H), 0.89 (t, J = 6.9 Hz, 6H); ^{13}C NMR (125.70 MHz, $CDCl_3$) δ 149.19, 142.25, 140.38, 134.96, 124.28, 123.90, 121.41, 37.01, 32.69, 31.87, 30.20, 30.03, 30.00, 23.51, 14.97. Anal calcd for: $C_{30}H_{40}O_4S_2$: C, 68.15; H, 7.63. Found: C, 67.95; H, 7.69. E-Factor: 136.

Method (2) To a solution of 2,7-dioctyl-[1]benzothieno[3,2-b][1]benzothiophene, (0.400 g, 0.860 mmol) in 20 mL of DCM, m-chloroperbenzoic acid (m-CPBA, 1.512 g, 6.75 mmol) was added stepwise at room temperature. The solution was stirred for 5 days. The white precipitate was removed by filtration and the organic solution was subsequently washed with a 10% aqueous $NaHSO_3$, a saturated solution of $NaHCO_3$, and brine. The dichloromethane was removed under reduced pressure. The crude product was purified by chromatography on silica gel (eluent: DCM/heptane 1:1). Crystallization from ethanol afforded the pure product as a bright yellow solid (0.230 g, 50%). E-factor = 1,650.

Computational Methods

The calculations have been performed using the ORCA suite of programs in a localized-basis-set framework. Kohn-Sham orbitals have been expanded on a ZORA-re-contracted def2-QZVPP Gaussian type basis set. Fully decontracted def2-QZVPP/J has also been used as an auxiliary basis set for Coulomb fitting in a resolution-of-identity/chain-of-spheres (RIJCOSX) framework. Molecular geometries have been fully optimized at the B3LYP and TPSSh level of theory, including dispersion forces calculated by using the DFT-D3 approach. TDDFT calculations have been performed by using the B3LYP functional and the same basis sets discussed above. A large basis of 300 vectors connecting occupied and unoccupied Kohn-Sham orbitals has been used for the calculations of the first 30 electronic transitions. The absorption and fluorescence vibrational structure has been calculated by using the independent mode displaced harmonic oscillator (IMDHO) model. The reduction potentials of the molecules have been calculated as discussed elsewhere. The molecules and their positive and negative ions have been embedded in an implicit CH_2Cl_2 solvent using the continuum-solvation model (COSMO) and fully optimized by using the TPSSh functional. The corresponding redox potentials have been calculated as ΔG values between neutral and charged species.

Cyclic Voltammetry

Cyclovoltammograms of BTBT-Ox_2 and BTBT-Ox CH_2Cl_2 solutions were acquired at 50 mV/ s in a scan range 0.8/−1.6 V and 0.9/−2.3 V, respectively, starting from the open-circuit voltage values (−0.28 V and 0.34 V, respectively) and applying oxidative potential. No oxidation waves were detected in the first cycles. HOMO and LUMO values were calculated from the onset of oxidative and reductive CV waves, respectively. The potential values of −4.67 V for NHE versus vacuum and of 0.63 V for Fc/Fc^+ versus NHE were used.

Optical Measurements

The sample optical absorption spectrum was recorded by a Varian Cary 50 spectrometer at normal incidence in dual beam mode, with a spectral resolution of 1 nm, using a quartz Suprasil cuvette with an optical path of 0.1 cm. The PL and excitation PL (PLE) spectra were recorded in continuous wave mode by a Varian Eclipse fluorimeter, with a spectral resolution of 2.5 nm. The PL has been monitored exciting the sample at 350 nm. The **C_8-BTBTOx_2-C_8** PL QY has been measured by relative methods using a 10^{-5} M solution of 9,10-diphenylanthracene (DPA) in THF (QY = 95%). Time-resolved PL data have been acquired using a pulsed laser at 355 nm as an excitation source. Thermal stability measurements were carried out in air using a 405 nm cw laser (incident power 20 mW) and collecting the emitted light with a TM-C10083CA Hamamatsu Mini-Spectrometer. The temperature was controlled using a GM200-71-14-16 Adaptive Power Management Peltier cell and monitored in real time with a K-type thermocouple.

Fabrication of the PMMA LSC

The PMMA waveguide was fabricated by bulk polymerization using the industrial cell-casting process. The process was characterized by two steps. First, the so-called "syrup" was prepared: the monomer, purified through a basic aluminum oxide column, was heated in a beaker to 80°C. When the MMA temperature stabilized, AIBN (100 ppm w/w with respect to MMA) was added. At that point, the prepolymerization (an exothermic process) took place and the monomer temperature increased up to the MMA boiling temperature (95°C); when the monomer achieved the stage of vigorous boiling, the syrup was quenched. In the second step, the prepolymer was degassed by four freeze-pump-thaw cycles in order to remove oxygen and

introduce argon atmosphere and then mixed with C_8-BTBTOx_2-C_8 in MMA containing lauryl peroxide (400 ppm w/w with respect to MMA) described above (10% w/w with respect to the syrup). Finally, the viscous liquid was introduced into the casting mold under argon flow where the polymerization reaction proceeded. Casting mold was made by two glass plates sealed with a polyvinyl chloride (PVC) gasket (in order to preserve the inert atmosphere) and clamped together. The clamps contained springs in order to accommodate the shrinkage of the polymer plate during the polymerization process. Casting mold was placed in a water bath at 55°C for 48 h. Finally, the slab was post-cured in the oven at 115°C overnight. The final waveguide was later cut to size and the edge was polished and optically coupled with c-Si PV cells. The optical output was measured in ambient illumination using a calibrated solar cell as a reference. The measurements were conducted on a dedicated test site. The device was mounted on a frame at ca. 1.5 m from the ground, and the ground surface was entirely coated with a black plastic mantle so as to minimize contributions by reflected/scattered transmitted or ambient light.

Monte Carlo Simulations

The simulations of the LSC were performed via a Monte Carlo ray-tracing method, in which the photon propagation follows the geometrical optics laws. Because the LSC thickness (0.7 cm) was much larger than the light coherence length, interference has been neglected. The stochastic nature of the simulations was reflected in the fact that the ray is transmitted or reflected with the probabilities proportional to respective energy fluxes given by Fresnel Laws. The dependence of these probabilities on the state of polarization of the incident ray (e.g., s- or p-polarized) was also considered. A specific event (i.e., transmission or reflection) was chosen according to a random Monte Carlo drawing. Monte Carlo ray-tracing simulations of the LSC were performed using the experimental absorption spectra of C_8-BTBT-Ox_2-C_8 in solution and its relative PL spectra. AM 1.5G solar spectrum was employed as the LSC excitation source. Once a photon was absorbed by a C_8-BTBT-Ox_2-C_8 molecule, the subsequent fate of the excitation (i.e., reemission or nonradiative relaxation) was again determined by the Monte Carlo sampling according to the emission QY set to Φ_{PL} = 95%). The direction of reemission was distributed uniformly, and the reemission wavelength was determined using the rejection sampling applied to the accurate PL spectra obtained from the experiment. The ultimate fate of each photon is either loss due to nonradiative recombination or escape from the LSC via one of the interfaces. A single-ray Monte Carlo simulation is typically repeated 10^6–10^7 times to have a proper statistical averaging. A stochastic nature of simulations allows one to easily evaluate LSCs performance, such as the OQE (edge-emitted photons per absorbed solar photons) and the OE (edge-emitted photons per impinging solar photons).

SUPPLEMENTAL INFORMATION

Supplemental Information can be found online at https://doi.org/10.1016/j.joule.2020.08.006.

ACKNOWLEDGMENTS

We thank the MIUR "Dipartimenti di Eccellenza 2017 Project – Materials for Energy" and the PRIN2017 BOOSTER (2017YXX8AZ) for financial support.

AUTHOR CONTRIBUTIONS

L.B. and S.B. conceived this study. S.M. and A.S. synthesized the compounds under the supervision of M.S. G.M. performed the calculations. A.M. and V.P. conducted

the spectroscopic characterization. R.R. and I.F. performed and interpreted the cyclovoltammetry measurements. S.B. planned and coordinated the device fabrication and testing. F.B. produced the LSC. F.M. performed the ray-tracing simulation. M.G. assembled and characterized the device. S.B. and L.B. wrote the paper in consultation with all authors.

DECLARATION OF INTERESTS

The authors declare no competing interests.

Received: April 30, 2020
Revised: June 29, 2020
Accepted: August 4, 2020
Published: September 1, 2020

REFERENCES

1. Debije, M.G., and Verbunt, P.P.C. (2012). Thirty years of luminescent solar concentrator research: solar energy for the built environment. Adv. Energy Mater. *2*, 12–35.
2. Meinardi, F., Bruni, F., and Brovelli, S. (2017). Luminescent solar concentrators for building-integrated photovoltaics. Nat. Rev. Mater. *2*, 17072.
3. Goetzberger, A., and Greube, W. (1977). Solar energy conversion with fluorescent collectors. Appl. Phys. *14*, 123–139.
4. Meinardi, F., McDaniel, H., Carulli, F., Colombo, A., Velizhanin, K.A., Makarov, N.S., Simonutti, R., Klimov, V.I., and Brovelli, S. (2015). Highly efficient large-area colourless luminescent solar concentrators using heavy-metal-free colloidal quantum dots. Nat. Nanotechnol. *10*, 878–885.
5. Meinardi, F., Ehrenberg, S., Dhamo, L., Carulli, F., Mauri, M., Bruni, F., Simonutti, R., Kortshagen, U., and Brovelli, S. (2017). Highly efficient luminescent solar concentrators based on earth-abundant indirect-bandgap silicon quantum dots. Nat. Photonics *11*, 177–185.
6. Meinardi, F., Colombo, A., Velizhanin, K.A., Simonutti, R., Lorenzon, M., Beverina, L., Viswanatha, R., Klimov, V.I., and Brovelli, S. (2014). Large-area luminescent solar concentrators based on 'Stokes-shift-engineered' nanocrystals in a mass-polymerized PMMA matrix. Nat. Photonics *8*, 392–399.
7. Anand, A., Zaffalon, M.L., Gariano, G., Camellini, A., Gandini, M., Brescia, R., Capitani, C., Bruni, F., Pinchetti, V., Zavelani-Rossi, M., et al. (2020). Evidence for the band-edge exciton of CuInS2 nanocrystals enables record efficient large-area luminescent solar concentrators. Adv. Funct. Mater. *30*, 1906629.
8. Hermann, A.M. (1982). Luminescent solar concentrators—a review. Sol. Energy *29*, 323–329.
9. Sark, W.G.J.H.Mv v., Barnham, K.W.J., Slooff, L.H., Chatten, A.J., Büchtemann, A., Meyer, A., McCormack, S.J., Koole, R., Farrell, D.J., Bose, R., et al. (2008). Luminescent Solar Concentrators - a review of recent results. Opt. Express *16*, 21773–21792.
10. Aste, N., Tagliabue, L.C., Del Pero, C., Testa, D., and Fusco, R. (2015). Performance analysis of a large-area luminescent solar concentrator module. Renew. Energy *76*, 330–337.
11. Beverina, L., and Sanguineti, A. (2013). Organic fluorophores for luminescent solar concentrators In Solar Cell Nanotechnology (John Wiley & Sons, Inc.), pp. 317–355.
12. Rowan, B.C., Wilson, L.R., and Richards, B.S. (2008). Advanced material concepts for luminescent solar concentrators. IEEE J. Select. Topics Quantum Electron. *14*, 1312–1322.
13. Slooff, L.H., Bende, E.E., Burgers, A.R., Budel, T., Pravettoni, M., Kenny, R.P., Dunlop, E.D., and Büchtemann, A. (2008). A luminescent solar concentrator with 7.1% power conversion efficiency. phys. stat. sol. (RRL) *2*, 257–259.
14. Erickson, C.S., Bradshaw, L.R., McDowall, S., Gilbertson, J.D., Gamelin, D.R., and Patrick, D.L. (2014). Zero-reabsorption doped-nanocrystal luminescent solar concentrators. ACS Nano *8*, 3461–3467.
15. Wu, K., Li, H., and Klimov, V.I. (2018). Tandem luminescent solar concentrators based on engineered quantum dots. Nat. Photonics *12*, 105–110.
16. Wei, M., de Arquer, F.P.G., Walters, G., Yang, Z., Quan, L.N., Kim, Y., Sabatini, R., Quintero-Bermudez, R., Gao, L., Fan, J.Z., et al. (2019). Ultrafast narrowband exciton routing within layered perovskite nanoplatelets enables low-loss luminescent solar concentrators. Nat. Energy *4*, 197–205.
17. Zhou, Y., Benetti, D., Fan, Z., Zhao, H., Ma, D., Govorov, A.O., Vomiero, A., and Rosei, F. (2016). Near infrared, highly efficient luminescent solar concentrators. Adv. Energy Mater. *6*, 1501913.
18. Altan Bozdemir, O., Erbas-Cakmak, S., Ekiz, O.O., Dana, A., and Akkaya, E.U. (2011). Towards unimolecular luminescent solar concentrators: Bodipy-based dendritic energy-transfer cascade with panchromatic absorption and monochromatized emission. Angew. Chem. Int. Ed. Engl. *50*, 10907–10912.
19. Banal, J.L., Ghiggino, K.P., and Wong, W.W.H. (2014). Efficient light harvesting of a luminescent solar concentrator using excitation energy transfer from an aggregation-induced emitter. Phys. Chem. Chem. Phys. *16*, 25358–25363.
20. Cambié, D., Zhao, F., Hessel, V., Debije, M.G., and Noël, T. (2017). A leaf-inspired luminescent solar concentrator for energy-efficient continuous-flow photochemistry. Angew. Chem. Int. Ed. Engl. *129*, 1070–1074.
21. Flores Daorta, S., Proto, A., Fusco, R., Claudio Andreani, L., and Liscidini, M. (2014). Cascade luminescent solar concentrators. Appl. Phys. Lett. *104*, 153901.
22. Schiphorst, J.t., Kendhale, A.M., Debije, M.G., Menelaou, C., Herz, L.M., and Schenning, A.P.H.J. (2014). Dichroic perylene bisimide triad displaying energy transfer in switchable luminescent solar concentrators. Chem. Mater. *26*, 3876–3878.
23. Yang, C., and Lunt, R.R. (2017). Limits of visibly transparent luminescent solar concentrators. Adv. Opt. Mater. *5*, 1600851.
24. Correia, S.F.H., de Zea Bermudez, V., Ribeiro, S.J.L., André, P.S., Ferreira, R.A.S., and Carlos, L.D. (2014). Luminescent solar concentrators: challenges for lanthanide-based organic–inorganic hybrid materials. J. Mater. Chem. A *2*, 5580–5596.
25. Sanguineti, A., Monguzzi, A., Vaccaro, G., Meinardi, F., Ronchi, E., Moret, M., Cosentino, U., Moro, G., Simonutti, R., Mauri, M., et al. (2012). NIR emitting ytterbium chelates for colourless luminescent solar concentrators. Phys. Chem. Chem. Phys. *14*, 6452.
26. Wang, X., Wang, T., Tian, X., Wang, L., Wu, W., Luo, Y., and Zhang, Q. (2011). Europium complex doped luminescent solar concentrators with extended absorption range from UV to visible region. Sol. Energy *85*, 2179–2184.
27. Meinardi, F., Akkerman, Q.A., Bruni, F., Park, S., Mauri, M., Dang, Z., Manna, L., and Brovelli, S. (2017). Doped halide perovskite nanocrystals for reabsorption-free luminescent solar concentrators. ACS Energy Lett *2*, 2368–2377.
28. Della Sala, P., Buccheri, N., Sanzone, A., Sassi, M., Neri, P., Talotta, C., Rocco, A., Pinchetti, V., Beverina, L., Brovelli, S., and Gaeta, C. (2019). First demonstration of the use of very large

Stokes shift cycloparaphenylenes as promising organic luminophores for transparent luminescent solar concentrators. Chem. Commun. *55*, 3160–3163.

29. Yang, C., Moemeni, M., Bates, M., Sheng, W., Borhan, B., and Lunt, R.R. (2020). High-performance near-infrared harvesting transparent luminescent solar concentrators. Adv. Optical Mater. *8*, 1901536.

30. Fattori, V., Melucci, M., Ferrante, L., Zambianchi, M., Manet, I., Oberhauser, W., Giambastiani, G., Frediani, M., Giachi, G., and Camaioni, N. (2011). Poly(lactic acid) as a transparent matrix for luminescent solar concentrators: a renewable material for a renewable energy technology. Energy Environ. Sci. *4*, 2849.

31. Griffini, G. (2019). Host matrix materials for luminescent solar concentrators: recent achievements and forthcoming challenges. Front. Mater. https://doi.org/10.3389/fmats.2019.00029.

32. Griffini, G., Brambilla, L., Levi, M., Del Zoppo, M., and Turri, S. (2013). Photo-degradation of a perylene-based organic luminescent solar concentrator: molecular aspects and device implications. Sol. Energy Mater. Sol. Cells *111*, 41–48.

33. G. Seybold and Strange, A. (1987). BASF AG. German Patent DE 3545004, filed December 19, 1985, and published June 25, 1987.

34. Sanzone, A., Calascibetta, A., Ghiglietti, E., Ceriani, C., Mattioli, G., Mattiello, S., Sassi, M., and Beverina, L. (2018). Suzuki–Miyaura micellar one-pot synthesis of symmetrical and unsymmetrical 4,7-diaryl-5,6-difluoro-2,1,3-benzothiadiazole luminescent derivatives in water and under air. J. Org. Chem. *83*, 15029–15042.

35. Scheinhardt, B., Trzaskowski, J., Baier, M.C., Stempfle, B., Oppermann, A., Wöll, D., and Mecking, S. (2013). Anisotropic polyethylene nanocrystals labeled with a single fluorescent dye molecule: Toward monitoring of nanoparticle orientation. Macromolecules *46*, 7902–7910.

36. Lipshutz, B.H., and Ghorai, S. (2014). Transitioning organic synthesis from organic solvents to water. What's your E factor? Green Chem *16*, 3660–3679.

37. Mattiello, S., Rooney, M., Sanzone, A., Brazzo, P., Sassi, M., and Beverina, L. (2017). Suzuki–Miyaura micellar cross-coupling in water, at room temperature, and under aerobic atmosphere. Org. Lett. *19*, 654–657.

38. Rooney, M., Mattiello, S., Stara, R., Sanzone, A., Brazzo, P., Sassi, M., and Beverina, L. (2018). Suzuki-Miyaura cross-coupling of latent pigments in water/toluene emulsion under aerobic atmosphere. Dyes Pigments *149*, 893–901.

39. Schweicher, G., Lemaur, V., Niebel, C., Ruzié, C., Diao, Y., Goto, O., Lee, W.Y., Kim, Y., Arlin, J.B., Karpinska, J., et al. (2015). Bulky end-capped (1)Benzothieno[3,2- b] benzothiophenes: reaching high-mobility organic semiconductors by fine tuning of the crystalline solid-state order. Adv. Mater. *27*, 3066–3072.

40. Borshchev, O.V., Sizov, A.S., Agina, E.V., Bessonov, A.A., and Ponomarenko, S.A. (2017). Synthesis of organosilicon derivatives of [1] benzothieno[3,2-b][1]-benzothiophene for efficient monolayer Langmuir–Blodgett organic field effect transistors. Chem. Commun. *53*, 885–888.

41. Combe, C.M.S., Biniek, L., Schroeder, B.C., and McCulloch, I. (2014). Synthesis of [1] benzothieno[3,2-b][1]benzothiophene pendant and norbornene random co-polymers via ring opening metathesis. J. Mater. Chem. C *2*, 538–541.

42. Barbarella, G., Favaretto, L., Sotgiu, G., Antolini, L., Gigli, G., Cingolani, R., and Bongini, A. (2001). Rigid-core oligothiophene-S,S-dioxides with high photoluminescence efficiencies both in solution and in the solid state. Chem. Mater. *13*, 4112–4122.

43. Di Maria, F., Fabiano, E., Gentili, D., Biasiucci, M., Salzillo, T., Bergamini, G., Gazzano, M., Zanelli, A., Brillante, A., Cavallini, M., et al. (2014). Polymorphism in crystalline microfibers of achiral Octithiophene: the effect on charge transport, supramolecular chirality and optical properties. Adv. Funct. Mater. *24*, 4943–4951.

44. Mattioli, G., Mattiello, S., Sassi, M., and Beverina, L. (2020). Ab initio simulations of interfaces between SAM-modified gold electrodes and n-type or p-type organic semiconductors based on the benzothieno-benzothiophene (BTBT) architecture. J. Phys. Chem. C *124*, 3601–3609.

45. Okamoto, K. (2011). Jpn. Kokai Tokkyo Koho patent JP 2011011977 A 20110120, filed June 30, 2009, and published January 20, 2011.

46. Andersen, J., and Mack, J. (2018). Mechanochemistry and organic synthesis: from mystical to practical. Green Chem *20*, 1435–1443.

47. Sanguineti, A., Sassi, M., Turrisi, R., Ruffo, R., Vaccaro, G., Meinardi, F., and Beverina, L. (2013). High Stokes shift perylene dyes for luminescent solar concentrators. Chem. Commun. *49*, 1618.

48. Turrisi, R., Sanguineti, A., Sassi, M., Savoie, B., Takai, A., Patriarca, G.E., Salamone, M.M., Ruffo, R., Vaccaro, G., Meinardi, F., et al. (2015). Stokes shift/emission efficiency trade-off in donor–acceptor perylenemonoimides for luminescent solar concentrators. J. Mater. Chem. A *3*, 8045–8054.

49. Debije, M.G., Teunissen, J.-P., Kastelijn, M.J., Verbunt, P.P.C., and Bastiaansen, C.W.M. (2009). The effect of a scattering layer on the edge output of a luminescent solar concentrator. Sol. Energy Mater. Sol. Cells *93*, 1345–1350.

50. Akkerman, Q.A., Gandini, M., Di Stasio, F., Rastogi, P., Palazon, F., Bertoni, G., Ball, J.M., Prato, M., Petrozza, A., and Manna, L. (2017). Strongly emissive perovskite nanocrystal inks for high-voltage solar cells. Nat. Energy *2*, 16194.